Nanoscale Advances

ROYAL SOCIETY OF CHEMISTRY

PAPER

View Article Online
View Journal | View Issue

Check for updates

Cite this: *Nanoscale Adv.*, 2023, **5**, 1706

Negatively charged $Cu_{1.33}S$ nanochains: endocytic pathway, photothermal therapy and toxic effect *in vivo*†

Le Luo and Zhenghua Wang *

Received 5th November 2022
Accepted 26th January 2023

DOI: 10.1039/d2na00776b

rsc.li/nanoscale-advances

Negatively charged nanomaterials have good biocompatibility and low cytotoxicity, but the efficiency of their entry into cells is relatively low. Thus, striking a balance between cell transport efficiency and cytotoxicity is a challenging problem in the field of nanomedicine. In this work, negatively charged $Cu_{1.33}S$ nanochains have shown a higher cellular uptake level in 4T1 cells than $Cu_{1.33}S$ nanoparticles with a similar diameter and surface charge. Inhibition experiments indicate that the cellular uptake of the nanochains depends principally on the lipid-raft protein (*i.e.* caveolin-1) mediated pathway, although the role of clathrin cannot be ruled out. Caveolin-1 can provide short-range attraction at the membrane interface. Furthermore, by using biochemical analysis, blood routine examination and histological evaluation on healthy Sprague Dawley rats, it is found that the $Cu_{1.33}S$ nanochains have no obvious toxic effect. The $Cu_{1.33}S$ nanochains have an effective photothermal therapy effect of tumor ablation *in vivo* under low injection dosage and laser intensity. As for the best performing group (20 μg + 1 W cm^{-2}), the temperature of the tumor site rapidly increases within the initial 3 min and rises to a plateau of 79 °C ($\Delta T = 46$ °C) at 5 min. These results reveal the feasibility of the $Cu_{1.33}S$ nanochains as a photothermal agent.

1. Introduction

In recent years, nanomaterials have been widely used in biomedical fields.[1–6] Nevertheless, due to the anionic nature of the cell membrane, these nanomaterials are often designed to be positively charged to overcome the electrostatic barrier.[7–9] However, because of cell-specific endocytic and mitochondrial injury, the positively charged nanomaterials may induce side effects affecting their biocompatibility, which in turn affects their potential clinical use.[10–14] By contrast, negatively charged nanomaterials have good biocompatibility and low cytotoxicity. Unfortunately, the efficiency of their entry into cells is relatively low.[15] Thus, striking a balance between cell transport efficiency and cytotoxicity is a challenging problem in the field of nanomedicine.

Fortunately, cell entry of negatively charged nanomaterials has been observed in some nanostructures, such as DNA cages,[16] hierarchical dendron–virus complexes,[17] and two-dimensional graphene oxide nanosheets.[18] For example, some self-assembled DNA nanostructures (icosahedral, tetrahedral, and autonomous DNA) can enter mammalian cell lines such as HeLa *via* receptor-mediated endocytosis, thus resulting in versatile therapeutic applications.[19,20] These reports have shown that nonspherical nanostructures may enter cells more efficiently than spherical nanoparticles.

In the past few decades, photothermal therapy has been diffusely used in cancer treatment and antibacterial fields.[21–26] Photothermal therapy offers a non-invasive therapy by making use of the photothermal effect of photothermal agents (PTAs). PTAs can convert the light energy of a near infrared (NIR) laser into heat to trigger the local hyperthermic ablation of cancer. The biological tissues can be transparent to the NIR laser, allowing deep tissue penetration.[27,28] One encouraging report is that Halas's group demonstrated the initial results of clinical trials in which gold-silica nanoshells were used in combination with magnetic resonance-ultrasound fusion imaging to focally ablate low-intermediate-grade tumors within the prostate.[29] For conducting safe and highly effective photothermal therapy under low power density and dosage, an ideal candidate PTA should meet two conditions at the same time, that is, high photothermal conversion efficiency in the NIR region and accumulation at the tumor site.[30]

$Cu_{2-x}S$ nanochains, with anisotropic one-dimensional (1D) assemblies and flexible features, are one form of nonspherical nanostructures with NIR absorption, of which the nano-bio interactions have not been investigated. Herein, we propose negatively charged $Cu_{1.33}S$ nanochains as an ideal PTA by demonstrating the endocytic pathway about uptake by 4T1 murine breast cancer cells (4T1 cells) *in vitro*, photothermal therapy effect and biosafety evaluations *in vivo*. The uptake

---

Key Laboratory of Functional Molecular Solids, Ministry of Education, College of Chemistry and Materials Science, Anhui Normal University, Wuhu 241000, People's Republic of China. E-mail: zhwang@ahnu.edu.cn

† Electronic supplementary information (ESI) available. See DOI: https://doi.org/10.1039/d2na00776b

value of $Cu_{1.33}S$ nanochains is 4.5 times higher than that of $Cu_{1.33}S$ nanoparticles in *in vitro* experiments, demonstrating the structural advantage of the nanochains. Inhibitor experiments showed that the caveolin-1 pathway plays a major role in the uptake of the nanochains by cells. Eventually, the recorded photothermal therapy for mice bearing 4T1 tumor with both low injection dosage and laser intensity is achieved. Furthermore, the "health" on healthy Sprague Dawley (SD) rats and pharmacokinetic evaluation on mice bearing tumor are applied to assess the clinical application prospect of the nanochains.

2. Experimental section

2.1 Synthesis of $Cu_{1.33}S$ nanochains and nanoparticles

The $Cu_{1.33}S$ nanochains (mean diameter = 8.7 nm) were synthesized according to our previously reported protocol.[31] An aqueous solution of $Cu_{1.33}S$ nanochains was obtained using a 0.016 : 12 : 36 : 6 molar ratio of [poly (sodium 4-styrenesulfonate) salt]/[$CuSO_4 \cdot 5H_2O$]/[ascorbic acid]/[thioacetamide], with a reaction time of 10 h at 30 °C. The final as-produced nanochain solution was a dark brown homogeneous aqueous dispersion.

The laser-induced synthesis of $Cu_{1.33}S$ nanoparticles involves two general steps, including preparation of $Cu_{1.33}S$ nanochains and subsequent disassemble into nanoparticles with similar diameter by laser irradiation. A typical synthesis procedure for the $Cu_{1.33}S$ nanoparticles was as follows: 1 mL nanochain aqueous solution was added into a centrifuge tube and then irradiated with a 1064 nm laser (0.32 W cm^{-2}) (MIL-N-1064 nm-5 W-CL20447) for more than 20 min in total. The attained solution was centrifuged at 8000 rpm for 15 min. The very little white sediment was removed, resulting in purified $Cu_{1.33}S$ nanoparticle solution. The final as-produced nanoparticle solution was a dark green homogeneous dispersion.

2.2 Cellular uptake of $Cu_{1.33}S$ nanochains and nanoparticles by 4T1 cells

Firstly, 4T1 cells were evenly dispersed and pre-seeded in 6-well plates. Then constant concentration $Cu_{1.33}S$ nanochains and nanoparticles were respectively added into different wells to co-incubate with the cells. Each experimental group included at least three wells ($n = 3$). On reaching a certain co-incubation time, the culture medium in the wells was discarded. The cells were gently washed with phosphate buffered saline (PBS) three times. After repeatedly frozen and thawed, the cells were digested with concentrated nitric acid (guaranteed reagent) for quantitative analysis by inductively coupled plasma mass spectrometry (ICP-MS).

2.3 Studies on the endocytosis pathway of $Cu_{1.33}S$ nanochains and nanoparticles

The 4T1 cells were pre-incubated with 450 mM sucrose (or 10 mM methyl-β-cyclodextrin) for 30 min. Then constant concentration $Cu_{1.33}S$ nanochains or nanoparticles were added to the cells to co-incubate for a certain time. During the entire experimental process, the inhibitors (sucrose or methyl-β-cyclodextrin) were retained in the culture medium.

2.4 Western blotting analysis

The expression levels of caveolin-1 after various treatments were analyzed by western blotting. RIPA Lysis Buffer was used to exact the cell membrane protein. The cell extracts were separated by 12% sodium dodecyl sulfate-polyacrylamide gel electrophoresis. The current and time during transfer onto the membrane were individually set as 200 mA and 50 min.

2.5 *In vivo* photothermal therapy of $Cu_{1.33}S$ nanochains

All animal procedures were performed in accordance with the Guidelines for Care and Use of Laboratory Animals of "SPF (Beijing) Biotechnology Co., Ltd" and experiments were approved by the Animal Ethics Committee of "SPF (Beijing) Biotechnology Co., Ltd". The volume of tumors in 8 week-old nude mice weighing 16 to 20 g grew to about 0.28 cm^3 by subcutaneous injection of 4T1 cells. The volume of the tumor was measured by using the following equation:

$$\text{Volume} = \text{length} \times \text{width} \times \text{height} \times \pi/6$$

The mice bearing 4T1 tumors were divided into five groups ($n = 3$) according to the different injection doses and laser power densities used in the experiments, as listed in Table 1. An 808 nm laser was used to irradiate the tumor sites of mice.

3. Results and discussion

3.1 Synthesis and characteristics of the $Cu_{1.33}S$ nanochains and nanoparticles

The $Cu_{1.33}S$ nanochains are prepared by a self-assembly strategy, as reported in our previous work.[31] For comparison, the nanoparticles are synthesized by disassemble the nanochains into nanoparticles under laser irradiation. As shown by the transmission electron microscope (TEM) image (Fig. 1A), the $Cu_{1.33}S$ nanochains show a curved chain-like nanostructure, with an average diameter of about 8.7 nm (Fig. S1†). The $Cu_{1.33}S$ nanoparticles synthesized by the laser-induced method have a similar diameter to the $Cu_{1.33}S$ nanochains (Fig. 1B). High-angle annular dark field scanning transmission electron microscopy (HAADF-STEM) and the corresponding elemental mapping images reveal that Cu and S elements are evenly distributed in the nanochains and nanoparticles (Fig. 1C and D). The energy-dispersive X-ray spectroscopy (EDS) spectra demonstrate that the as-produced nanochains and nanoparticles have the same Cu : S ratio (Fig. S2 and S3†). Furthermore, the composition and valence states of the elements in both the nanochains and nanoparticles are studied by X-ray photoelectron spectroscopy (XPS) and Auger electron spectroscopy (AES) (Fig. S4†). The Cu and S peaks can be observed in the XPS survey spectra (Fig. S4A†). The peak positions in the Cu 2p region of the nanochains are close to the peaks for the nanoparticles (Fig. S4B†). The Cu $2p_{3/2}$ and Cu $2p_{1/2}$ peaks of both the

Table 1 The grouping of the experimental mice

Serial number of the groups	Named groups	Drugs by injection	Injection dosage	Laser power density
Control group	Saline + 0.75 W cm^{-2}	Saline	100 μL	0.75 W cm^{-2}
Group 1	20 μg + 1 W cm^{-2}	$Cu_{1.33}S$ nanochains	100 μL containing 20 μg Cu	1 W cm^{-2}
Group 2	20 μg + 0.75 W cm^{-2}	$Cu_{1.33}S$ nanochains	100 μL containing 20 μg Cu	0.75 W cm^{-2}
Group 3	14 μg + 0.75 W cm^{-2}	$Cu_{1.33}S$ nanochains	100 μL containing 14 μg Cu	0.75 W cm^{-2}
Group 4	7 μg + 0.75 W cm^{-2}	$Cu_{1.33}S$ nanochains	100 μL containing 7 μg Cu	0.75 W cm^{-2}

nanochains and nanoparticles can be fitted into two groups of peaks, indicating the coexistence of Cu^{2+} and Cu^{+}. And the fitted peak area ratio of the two samples is similar, suggesting that the Cu valence in the $Cu_{1.33}S$ nanochains and nanoparticle is similar. According to the AES spectrum (Fig. S4C†), the possibility of existing Cu(0) is excluded.[32,33] The peaks in the S 2p region can be fitted into four peaks (Fig. S4D†), which correspond to copper sulfide and sulfur in sulfate.[31] Note that the atomic ratio of Cu/S of the nanoparticles is found to be approximately 1.33, which further confirms that the composition of the nanochains and nanoparticles is similar.

As shown in the visible-NIR (vis-NIR) absorbance spectra (Fig. 2A), the $Cu_{1.33}S$ nanochains display a broad absorbance range from 550 to over 1300 nm. Compared with the $Cu_{1.33}S$ nanoparticles, the maximum peak of the $Cu_{1.33}S$ nanochains redshifts (Table S1†). Nanomaterials with a distinct absorption peak in the NIR region are perfect candidates as PTAs.[34] Due to the existence of poly (sodium 4-styrenesulfonate) salt that serves as the stabilizing ligand, the overall surface charge of both the $Cu_{1.33}S$ nanochains and nanoparticles is negative. Their zeta potential values are tested to be −46.8 (nanochains) and −41.8 mV (nanoparticles) by dynamic light scattering, respectively (Fig. 2B).

3.2 *In vitro* cellular uptake of the $Cu_{1.33}S$ nanochains and nanoparticles by 4T1 cells

To investigate the cellular uptake level of the $Cu_{1.33}S$ nanochains and nanoparticles, the 4T1 cells co-incubated with the

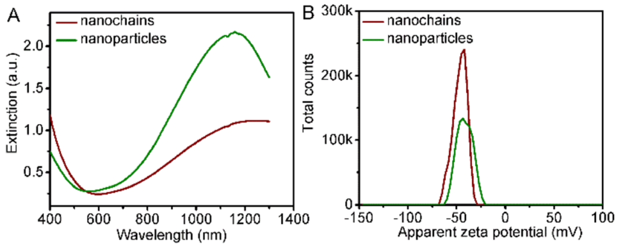

Fig. 2 (A) Vis-NIR absorbance spectra and (B) zeta potential values of the $Cu_{1.33}S$ nanochains and nanoparticles.

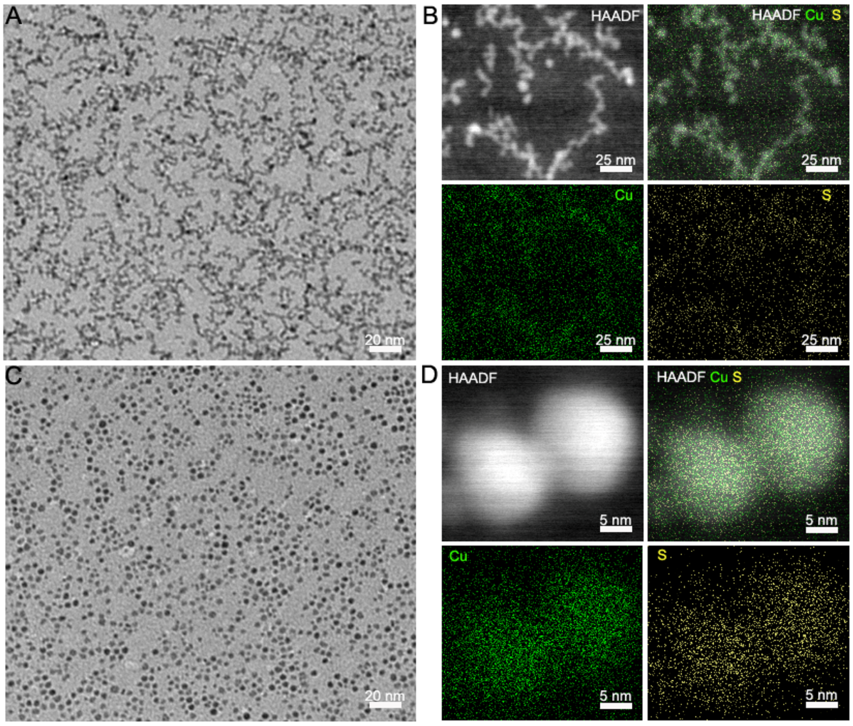

Fig. 1 (A) TEM image, (B) HAADF-STEM and corresponding elemental mapping images of the $Cu_{1.33}S$ nanochains. (C) TEM image, (D) HAADF-STEM and corresponding elemental mapping images of the $Cu_{1.33}S$ nanoparticles.

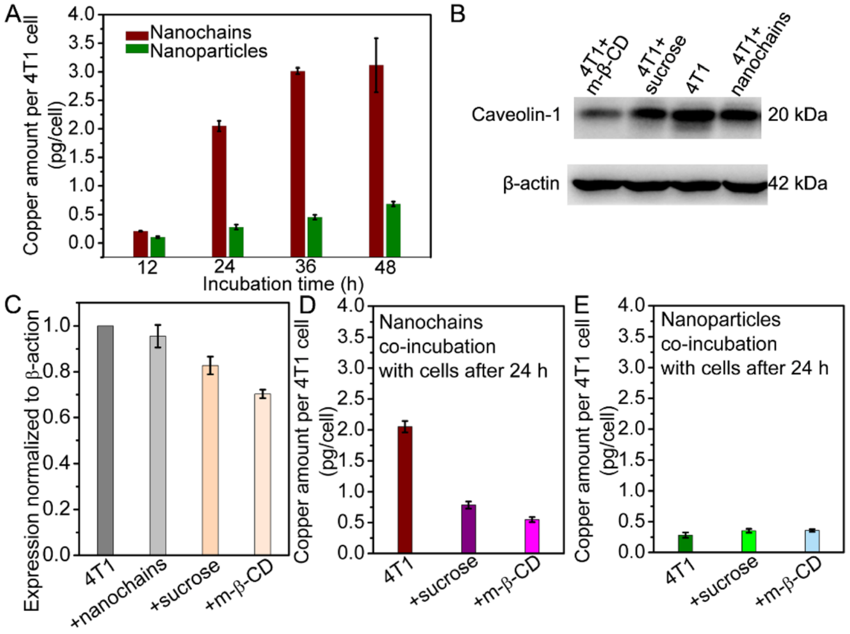

Fig. 3 (A) Quantitative analysis of intracellular copper content for the $Cu_{1.33}S$ nanochains and nanoparticles. (B) The caveolin-1 expression of cells before and after being treated with inhibitors examined by using the western blotting image and (C) gray scale analysis of protein bands with β-actin as the loading control. (D) Quantitative analysis of intracellular copper content for the $Cu_{1.33}S$ nanochains by 4T1 cells treated with inhibitors. (E) Quantitative analysis of intracellular copper content for the $Cu_{1.33}S$ nanoparticles by using 4T1 cells treated with inhibitors.

nanochains or nanoparticles are handled by repeated freezing and thawing. ICP-MS is used to quantitatively analyze the intracellular copper contents. As Fig. 3A shows, the uptake value of the $Cu_{1.33}S$ nanochains and nanoparticles increases with prolonging the co-incubation time. The maximal uptake values of $Cu_{1.33}S$ nanochains and nanoparticles are respectively 3.12 and 0.69 pg copper per cell at a co-incubation time of 48 h. Obviously, the $Cu_{1.33}S$ nanochains can be effectively taken up by 4T1 cells. And the uptake value of $Cu_{1.33}S$ nanochains is 4.5 times higher than that of $Cu_{1.33}S$ nanoparticles. The efficient cellular uptake of $Cu_{1.33}S$ nanochains is an interesting phenomenon.

The PSS modified $Cu_{1.33}S$ nanochains are intrinsically negatively charged in aqueous solution and are traditionally regarded to have low cell transport efficiency. We next studied the cell entry pathway of $Cu_{1.33}S$ nanochains and $Cu_{1.33}S$ nanoparticles. To determine the endocytosis pathway, we applied inhibitors to selectively block one of the pathways. M-β-CD is an inhibitor for the caveolae-mediated pathway by depleting cholesterol and disrupting caveolae,[35,36] while sucrose is an inhibitor for the clathrin-mediated pathway.[37,38] The expression of caveolin-1 in cells before and after being treated with inhibitors is measured by western blotting. The inhibited expression proportions of caveolin-1 are determined to be 28% and 15% by m-β-CD or sucrose, respectively (Fig. 3B and C). The inhibited proportions of endocytosis of nanochains are shown in Fig. 3D. The uptake of $Cu_{1.33}S$ nanochains is greatly reduced by 73% after treating the 4T1 cells with m-β-CD. Meanwhile, with the treatment by using sucrose, the uptake of $Cu_{1.33}S$ nanochains is suppressed by 62%. In contrast, after treating the cells with m-β-CD or sucrose, the uptake level of $Cu_{1.33}S$ nanoparticles slightly increases (Fig. 3E).

Inhibition experiments show that the cellular uptake of the $Cu_{1.33}S$ nanochains depends principally on the lipid-raft protein (*i.e.* caveolin-1) mediated pathway, although the role of clathrin cannot be ruled out. Having elucidated the biochemical mechanism of $Cu_{1.33}S$ nanochain uptake, combined with the underlying physical mechanism for like-charge attraction,[39,40] the cellular uptake process of the $Cu_{1.33}S$ nanochains can be described as follows: the negatively charged cell membrane is essentially a semi-fluid membrane consisting of unevenly distributed neutrally, negatively, and positively charged lipids.[40] Upon approaching the membrane, nanochains push away the negatively charged lipids and draw close the positively charged molecules, resulting in charge redistribution in the semifluidic membrane. And then, caveolin-1 can provide short-range attraction for endocytosing the nanochains, as shown in Scheme 1.

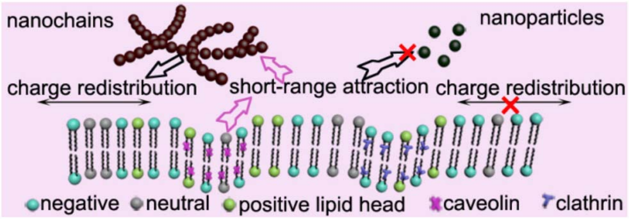

Scheme 1 Schematic illustration of the cellular uptake mechanism of the $Cu_{1.33}S$ nanochains and nanoparticles.

3.3 *In vivo* toxic effects and pharmacokinetics of the $Cu_{1.33}S$ nanochains

Next, the possible side effects of the $Cu_{1.33}S$ nanochains are evaluated through biochemistry analysis and blood routine examination on healthy SD rats intravenously injected with the nanochain solution (300 μL containing 97 μg Cu) by the tail-veil. The biochemistry index values, the rats' liver function markers, *i.e.* alanine aminotransferase, and aspartate aminotransferase numerical values, are constant in the normal range after nanochain injection, showing that the nanochains have no hepatic toxicity. The other markers, including total protein, albumin, creatinine, and uric acid, which are the main indices of renal function, also are constant in the normal range, suggesting that the kidney of rats has good function after nanochain injection (Fig. S5†).

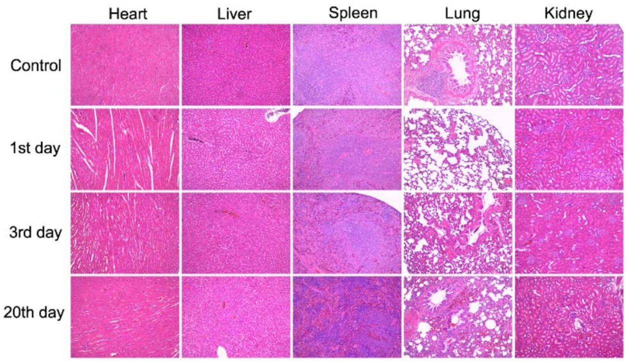

Fig. 4 H&E stained images of the major organs collected from rats intravenously injected with $Cu_{1.33}S$ nanochains on different days. Age-matched untreated rats are employed as the control.

The hematological evaluation is determined by blood routine examination (Fig. S6†). The white blood and platelet counts are reduced within a relatively short time (initial three days), but can recover to the normal level over 20 days. There is no distinct difference in all values of red blood cells between the control group and nanochain treated groups.

Furtherly, hematoxylin and eosin (H&E) staining analysis reveals that the structural patterns of the major organs of the treated groups have no obvious organ abnormalities and lesions compared with those of the control group (Fig. 4 and S7†). According to the above systematic evaluation, the $Cu_{1.33}S$ nanochains show trivial side effects and systemic toxicity on the health of rats.

Then, blood is drawn from the abdominal aorta of healthy SD rats injected with nanochain (300 μL containing 92.7 μg Cu) saline solution *via* the tail-vein. The blood circulation data fit a two-compartment model pharmacokinetic profile.[41] The half time of blood circulation is calculated to be 2.618 h (Fig. 5A).

The accumulation of nanochains in the tumor and the major organs of 4T1 tumor-bearing mice are determined after being intravenously injected with nanochains (200 μL containing 64.8 μg Cu) *via* the tail-vein (Fig. 5B). The tumor accumulation value of $Cu_{1.33}S$ nanochains reaches a relatively high level, 15% ID g^{-1} at 24 h post injection, compared to other reports as listed in Table S2.† To visualize the tumor accumulation of $Cu_{1.33}S$ nanochains, the bio-TEM images are taken to show the original appearance of nanochains in the tumor slice (Fig. 5C–E and S8–10†). A uniform distribution of the nanochains in tumor tissues is observed. The accumulation of nanochains at tumor sites is consistent with the results of quantitative analysis.

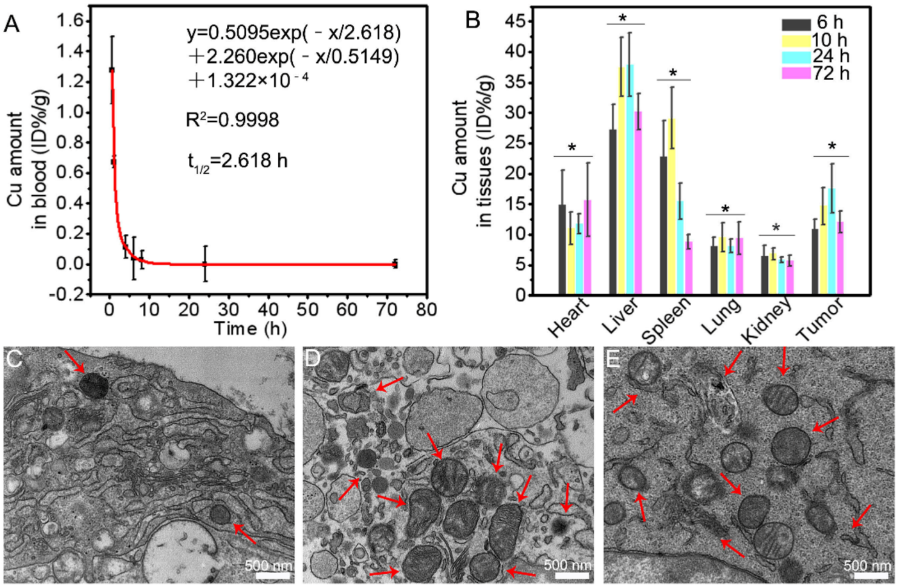

Fig. 5 (A) Blood circulation profile of the $Cu_{1.33}S$ nanochains in healthy SD rats. (B) Quantitative analysis for biodistribution of the $Cu_{1.33}S$ nanochains in the mice bearing 4T1 tumors. Bio-TEM images for showing tumor accumulation of the $Cu_{1.33}S$ nanochains, (C) 6 h, (D) 10 h, and (E) 24 h post intravenous injection. Data are presented as the mean ± SD, $n = 3$, one-way ANOVA Tukey's post-injection, and * denotes the statistical difference at $p < 0.05$.

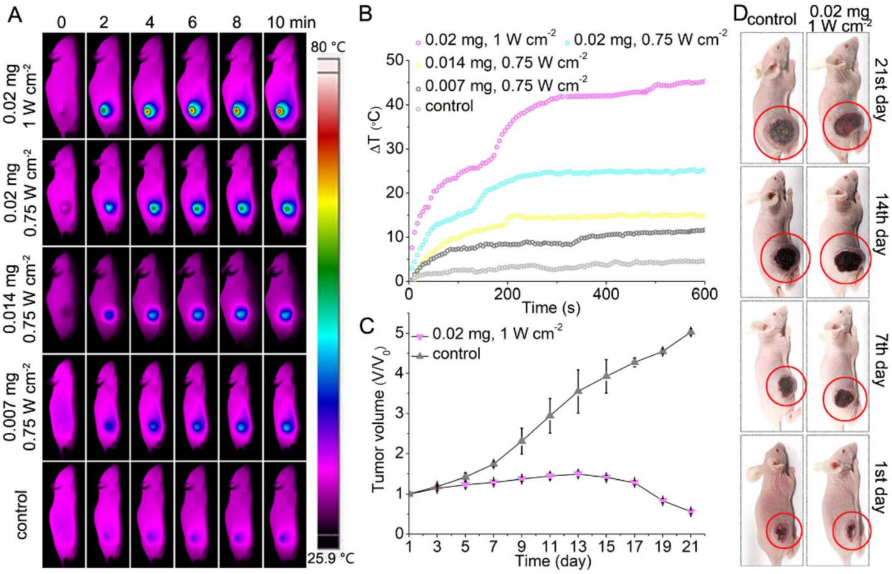

Fig. 6 (A) Infrared thermal images and (B) the temperature profiles for the tumor site surface of tumor-bearing mice recorded during the laser irradiation. (C) Tumor growth inhibition profiles and (D) corresponding photographs as a function of time post treatment. Data are presented as mean ± SD, and $n = 3$.

3.4 *In vivo* photothermal therapy of the $Cu_{1.33}S$ nanochains

In our previously published paper, we have calculated the photothermal conversion efficiency of $Cu_{1.33}S$ nanochains as 80.7% under an 808 nm laser (0.75 W cm^{-2}).[31] Here, the photothermal therapy effect of the nanochains on subcutaneous mouse tumor models is tested. When the tumor volume reaches about 0.28 cm^3, the mice bearing 4T1 tumors are randomly divided to five groups (three mice per group) according to the injection dosage and laser intensity (see the Experimental section). All tumor sites are then irradiated with an 808 nm laser for 10 min, with a thermal camera monitoring the local temperature in real time. Compared with control group mice injected with an equal volume of saline solution, the local temperatures of mice injected with the nanochains have obviously increased, even in group 4 (7 μg + 0.75 W cm^{-2}), as demonstrated by Fig. 6A and B. As for the best performing group (20 μg + 1 W cm^{-2}), the temperature of the tumor site rapidly increases within the initial 3 min, and then rises to a plateau of 79 °C ($\Delta T = 46$ °C) at 5 min (Movie S1†). As shown in Movie S1,† under the irradiation of a laser, a thermal spot at the tumor site appears. With the extension of the irradiation time, the thermal spot quickly brightens, demonstrating the rapid increase of the temperature of the tumor site.

To observe the photothermal therapy effects, the tumor growth curves are tracked and are shown in Fig. 6C. After treatment, the tumor volume of the control group mice (saline + 0.75 W cm^{-2}) gradually increases. On the 21st day, the tumor volume is 4.9 times bigger than that before treatment. In contrast, the tumor growth in group 1 (20 μg + 1 W cm^{-2}) is suppressed after treatment. And then, the tumor gradually dwindles and eventually disappears after 21 days, indicating effective photothermal therapy performance. The real photos of mice before and after treatment in different groups are shown in Fig. 6D. These phenomena are even better than those of previously reported PTAs (Table S3†). These results prove that $Cu_{1.33}S$ nanochains can be applied as highly efficient and safe PTAs *in vivo* with a low injection dosage (100 μL containing 20 μg Cu) and low laser intensity (1 W cm^{-2}).

4. Conclusions

In summary, we propose $Cu_{1.33}S$ nanochains as a candidate PTA with effective cellular uptake *in vitro* and a safe and efficient photothermal therapy effect of tumor ablation *in vivo*. *In vitro* experiments show that the negatively charged $Cu_{1.33}S$ nanochains have higher cellular uptake by 4T1 cells than $Cu_{1.33}S$ nanoparticles with a similar diameter and surface charge. According to the results of inhibition experiments, the cellular uptake of the $Cu_{1.33}S$ nanochains depends principally on the lipid-raft protein (*i.e.* caveolin-1) mediated pathway, although the role of clathrin cannot be ruled out. By using biochemical analysis, blood routine examination and histological evaluation on healthy SD rats, the $Cu_{1.33}S$ nanochains have no obvious toxic effect. In addition, pharmacokinetics and biodistribution experiments demonstrate that due to long blood circulation, the $Cu_{1.33}S$ nanochains have a high tumor accumulation level, compared to the reported PTAs. *In vivo* experiments demonstrate that the $Cu_{1.33}S$ nanochains with a low injection dosage (20 μg Cu) can exhibit an effective photothermal therapy effect on tumor ablation under low laser intensity (1 W cm^{-2}). All the results support that the $Cu_{1.33}S$ nanochains can be an advanced PTA.

Author contributions

Le Luo: conceptualization (equal); data curation (lead); formal analysis (equal); methodology (equal); investigation (equal);

writing-original draft (lead). Zhenghua Wang: conceptualization (equal); funding acquisition (lead); supervision (lead); writing-review and editing (lead).

Conflicts of interest

There are no conflicts to declare.

Acknowledgements

The work is supported by the National Natural Science Foundation of China (21671007). We also thank the Key Laboratory of Non-coding RNA Transformation Research of Anhui Higher Education Institution, and Central Laboratory in the First Affiliated Hospital of Wannan Medical College (Yijishan Hospital of Wannan Medical College) for help with western blotting.

References

1 B. R. Smith, E. E. B. Ghosn, H. Rallapalli, J. A. Prescher, T. Larson, L. A. Herzenberg and S. S. Gambhir, Selective uptake of single-walled carbon nanotubes by circulating monocytes for enhanced tumour delivery, *Nat. Nanotechnol.*, 2014, **9**, 481–487.

2 S. Kaida, H. Cabral, M. Kumagai, A. Kishimura, Y. Terada, M. Sekino, I. Aoki, N. Nishiyama, T. Tani and K. Kataoka, Visible drug delivery by supramolecular nanocarriers directing to single-platformed diagnosis and therapy of pancreatic tumor model, *Cancer Res.*, 2010, **70**, 7031–7041.

3 G. Lin, P. Mi, C. C. Chu, J. Zhang and G. Liu, Inorganic Nanocarriers overcoming multidrug resistance for cancer theranostics, *Adv. Sci.*, 2016, **3**, 1600134.

4 H. Ejima, J. J. Richardson and F. Caruso, Metal-phenolic networks as a versatile platform to engineer nanomaterials and biointerfaces, *Nano Today*, 2017, **12**, 136–148.

5 L. Tang, X. J. Yang, Q. Yin, K. M. Cai, H. Wang, I. Chaudhury, C. Yao, Q. Zhou, M. Kwon, J. A. Hartman, I. T. Dobrucki, L. W. Dobrucki, L. B. Borst, S. Lezmi, W. G. Helferich, A. L. Ferguson, T. M. Fan and J. J. Cheng, Investigating the optimal size of anticancer nanomedicine, *Proc. Natl. Acad. Sci. U. S. A.*, 2014, **111**, 15344–15349.

6 Y. Matsumoto, J. W. Nichols, K. Toh, T. Nomoto, H. Cabral, Y. Miura, R. J. Christie, N. Yamada, T. Ogura, M. R. Kano, Y. Matsumura, N. Nishiyama, T. Yamasoba, Y. H. Bae and K. Kataoka, Vascular bursts enhance permeability of tumour blood vessels and improve nanoparticle delivery, *Nat. Nanotechnol.*, 2016, **11**, 533–538.

7 Y. J. Liu, Z. T. Wang, Y. Liu, G. Z. Zhu, O. Jacobson, X. Fu, R. L. Bai, X. Y. Lin, N. Lu, X. Y. Yang, W. P. Fan, J. B. Song, Z. Wang, G. C. Yu, F. W. Zhang, H. Kalish, G. Niu, Z. H. Nie and X. Y. Chen, Suppressing nanoparticle-mononuclear phagocyte system interactions of two-dimensional gold nanorings for improved tumor accumulation and photothermal ablation of tumors, *ACS Nano*, 2017, **11**, 10539–10548.

8 O. P. Perumal, R. Inapagolla, S. Kannan and R. M. Kannan, The effect of surface functionality on cellular trafficking of dendrimers, *Biomaterials*, 2008, **29**, 3469–3476.

9 E. C. Cho, J. W. Xie, P. A. Wurm and Y. N. Xia, Understanding the role of surface charges in cellular adsorption *versus* internalization by selectively removing gold nanoparticles on the cell surface with a I2/KI etchant, *Nano Lett.*, 2009, **9**, 1080–1084.

10 T. Xia, M. Kovochich, M. Liong, J. I. Zink and A. E. Nel, Cationic polystyrene nanosphere toxicity depends on cell-specific endocytic and mitochondrial injury pathways, *ACS Nano*, 2008, **2**, 85–96.

11 A. C. Hunter and S. M. Moghimi, Cationic carriers of genetic material and cell death: a mitochondrial tale, *Biochim. Biophys. Acta*, 2010, **1797**, 1203–1209.

12 P. Symonds, J. C. Murray, A. C. Hunter, G. Debska, A. Szewczyk and S. M. Moghimi, Low and high molecular weight poly(L-lysine)s/poly(L-lysine)-DNA complexes initiate mitochondrial-mediated apoptosis differently, *FEBS Lett.*, 2005, **579**, 6191–6198.

13 S. M. Moghimi and H. M. Patel, Modulation of murine liver macrophage clearance of liposomes by diethylstilbestrol, The effect of vesicle surface charge and a role for the complement receptor Mac-1 (CD11b/CD18) of newly recruited macrophages in liposome recognition, *J. Controlled Release*, 2002, **78**, 55–65.

14 T. Xia, M. Kovochich, J. Brant, M. Hotze, J. Sempf, T. Oberley, C. Sioutas, J. I. Yeh, M. R. Wiesner and A. E. Nel, Comparison of the abilities of ambient and manufactured nanoparticles to induce cellular toxicity according to an oxidative stress paradigm, *Nano Lett.*, 2006, **6**, 1794–1807.

15 I. Canton and G. Battaglia, Endocytosis at the nanoscale, *Chem. Soc. Rev.*, 2012, **41**, 2718–2739.

16 A. S. Walsh, H. F. Yin, C. M. Erben, M. J. A. Wood and A. J. Turberfield, DNA cage delivery to mammalian cells, *ACS Nano*, 2011, **5**, 5427–5432.

17 M. A. Kostiainen, O. Kasyutich, J. J. L. M. Cornelissen and R. J. M. Nolte, Self-assembly and optically triggered disassembly of hierarchical dendron-virus complexes, *Nat. Chem.*, 2010, **2**, 394–399.

18 X. M. Sun, Z. Liu, K. Welsher, J. T. Robinson, A. Goodwin, S. Zaric and H. J. Dai, Nano-graphene oxide for cellular imaging and drug delivery, *Nano Res.*, 2008, **1**, 203–212.

19 D. Bhatia, S. Surana, S. Chakraborty, S. P. Koushika and Y. Krishnan, A synthetic icosahedral DNA-based host-cargo complex for functional *in vivo* imaging, *Nat. Commun.*, 2011, **2**, 339.

20 T. L. Halo, K. M. McMahon, N. L. Angeloni, Y. Xu, W. Wang, A. B. Chinen, D. Malin, E. Strekalova, V. L. Cryns, C. H. Cheng, C. A. Mirkin and C. S. Thaxton, NanoFlares for the detection, isolation, and culture of live tumor cells from human blood, *Proc. Natl. Acad. Sci. U. S. A.*, 2014, **111**, 17104–17109.

21 W. J. Shi, J. X. An, H. Tan, M. R. Jia and H. Gao, A biomimetic nonantibiotic nanoplatform for low-temperature photothermal treatment of urinary tract infections caused

by uropathogenic escherichia coli, *Adv. Healthcare Mater.*, 2022, **11**, 2101.

22 Y. F. Wang, H.-M. Meng and Z. H. Li, Near-infrared inorganic nanomaterial-based nanosystems for photothermal therapy, *Nanoscale*, 2021, **13**, 8751.

23 J. Qiao, X. F. Li and L. Qi, Fluorescent polymer-modified gold nanobipyramids for temperature sensing during photothermal therapy in living cells, *Chin. Chem. Lett.*, 2022, **33**, 3193–3196.

24 J. Yang, L. Xu, Y. Ding, C. Liu, B. C. Wang, Y. C. Yu, C. Hui and S. Ramakrishna, NIR-II-triggered composite nanofibers to simultaneously achieve intracranial hemostasis, killing superbug and residual cancer cells in brain tumor resection surgery, *Adv. Fiber Mater.*, 2023, **5**, 209–222.

25 B. Zhang, Y. Gao, R. Yang, Z. Ouyang, H. Yu, H. Wang and X. Shi, Tumor-anchoring drug-loaded fibrous microspheres for MRimaging-guided local chemotherapy and metastasis inhibition, *Adv. Fiber Mater.*, 2022, **4**, 807–819.

26 L. Chen, X. Sun, K. Cheng, P. D. Topham, M. Xu, Y. Jia, D. Dong, S. Wang, Y. Liu, L. Wang and Q. Yu, Temperature-regulating phase change fiber scaffold toward mild photothermal-chemotherapy, *Adv. Fiber Mater.*, 2022, **4**, 1669–1684.

27 P. Wang, L. M. Zhang, W. F. Zheng, L. M. Cong, Z. R. Guo, Y. Z. Y. Xie, L. Wang, R. B. Tang, Q. Feng, Y. Hamada, K. Gonda, Z. J. Hu, X. C. Wu and X. Y. Jiang, Thermo-triggered release of CRISPR-Cas9 system by lipid encapsulated gold nanoparticles for tumor therapy, *Angew. Chem., Int. Ed.*, 2018, **57**, 1491–1496.

28 D. Y. Li, E. Ha, J. G. Zhang, L. Y. Wang and J. Q. Hu, A synergistic chemodynamic-photodynamic-photothermal therapy platform based on biodegradable Ce-doped MoOx nanoparticles, *Nanoscale*, 2022, **14**, 14471–14481.

29 A. R. Rastinehada, H. Anastosa, E. Wajswola, J. S. Winokera, J. P. Sfakianosa, S. K. Doppalapudia, M. R. Carrickb, C. J. Knauera, B. Taoulib, S. C. Lewisb, A. K. Tewaria, J. A. Schwartzc, S. E. Canfieldd, A. K. Georgee, J. L. Westf and N. J. Halas, Gold nanoshell-localized photothermal ablation of prostate tumors in a clinical pilot device study, *Proc. Natl. Acad. Sci. U. S. A.*, 2019, **116**, 18590–18596.

30 J.-Q. Li, R.-X. Zhao, F.-M. Yang, X.-T. Qi, P.-K. Ye and M. Xie, An erythrocyte membrane-camouflaged biomimetic nanoplatform for enhanced chemo-photothermal therapy of breast cancer, *J. Mater. Chem. B*, 2022, **10**, 2047–2056.

31 L. Luo and Z. H. Wang, Self-assembled $Cu_{2-x}S$ nanochains network with tunable diameters for efficient photothermal conversion, *J. Alloys Compd.*, 2022, **910**, 164958.

32 D. Mott, J. Yin, M. Engelhard, R. Loukrakpam, P. Chang, G. Miller, I. Bae, N. C. Das, C. Wang, J. Luo and C. J. Zhong, From ultrafine thiolate-capped copper nanoclusters toward copper sulfide nanodiscs: a thermally activated evolution route, *Chem. Mater.*, 2010, **22**, 261–271.

33 G. X. Ma, Y. L. Zhou, X. Y. Li, K. Sun, S. Q. Liu, J. Q. Hu and N. A. Kotov, Self-assembly of copper sulfide nanoparticles into nanoribbons with continuous crystallinity, *ACS Nano*, 2013, **7**, 9010–9018.

34 A. Vogel and V. Venugopalan, Mechanisms of pulsed laser ablation of biological tissues, *Chem. Rev.*, 2003, **103**, 577.

35 B. Brandenburg and X. W. Zhuang, Virus trafficking–learning from single-virus tracking, *Nat. Rev. Microbiol.*, 2007, **5**, 197.

36 M. G. Qaddoumi, H. Veda, J. Yang, J. Davda, V. Labhasetwar and V. H. L. Lee, The characteristics and mechanisms of uptake of PLGA nanoparticles in rabbit conjunctival epithelial cell layers, *Mol. Vision, Pharm. Res.*, 2004, **21**, 641–648.

37 J. E. Heuser and R. G. W. Anderson, Hypertonic media inhibit receptor-mediated endocytosis by blocking clathrin-coated pit formation, *J. Cell Biol.*, 1989, **108**, 389.

38 L. Liang, J. Li, Q. Li, Q. Huang, J. Y. Shi, H. Yan and C. H. Fan, Single-particle tracking and modulation of cell entry pathways of a tetrahedral DNA nanostructure in live cells, *Angew. Chem., Int. Ed.*, 2014, **53**, 7745–7750.

39 A. E. Larsen and D. G. Grier, Like-charge attractions in metastable colloidal crystallites, *Nature*, 1997, **385**, 230–233.

40 H. M. Ding, J. Li, N. Chen, X. J. Hu, X. F. Yang, L. J. Guo, Q. Li, X. L. Zuo, L. H. Wang, Y. Q. Ma and C. H. Fan, DNA nanostructure-programmed like-charge attraction at the cell-membrane interface, *ACS Cent. Sci.*, 2018, **4**, 1344–1351.

41 G. S. Song, X. C. Zheng, Y. J. Wang, X. Xia, S. Chu and J. H. Rao, A magneto-optical nanoplatform for multimodality imaging of tumors in mice, *ACS Nano*, 2019, **13**, 7750–7758.